

Digging into the chemical complexity in the outer Galaxy: A hot molecular core in Sharpless 2-283

TOKI IKEDA,¹ TAKASHI SHIMONISHI,² HIROYUKI KANEKO,³ KENJI FURUYA,^{4,5} KEI E. I. TANAKA,⁶ AND NATSUKO IZUMI⁷

¹Department of Natural Environmental Science, Graduate School of Science and Technology, Niigata University, Ikarashi-nincho 8050, Nishi-ku, Niigata 950-2181, Japan

²Institute of Science and Technology, Niigata University, Ikarashi-nincho 8050, Nishi-ku, Niigata 950-2181, Japan

³College of Creative Studies, Niigata University, 8050 Ikarashi 2-no-cho, Nishi-ku, Niigata, Niigata 950-2181, Japan

⁴Department of Astronomy, Graduate School of Science, University of Tokyo, Tokyo 113-0033, Japan

⁵RIKEN Pioneering Research Institute, 2-1 Hirosawa, Wako-shi, Saitama 351-0198, Japan

⁶Department of Earth and Planetary Sciences, Institute of Science Tokyo, Meguro, Tokyo, 152-8551, Japan

⁷National Astronomical Observatory of Japan, 2-21-1 Osawa, Mitaka, Tokyo 181-8588, Japan

ABSTRACT

The outer Galaxy (galactocentric distance $\gtrsim 13.5$ kpc) serves as an excellent laboratory for investigating the chemical complexity in low-metallicity environments. Here, we present the chemical analyses for the outer Galactic hot core Sh 2-283-1a SMM1 ($D_{\text{GC}} = 15.7$ kpc and $Z \sim 0.3 Z_{\odot}$), recently detected by Ikeda et al. (2025) using ALMA. Toward this source, a variety of molecular species, including complex organic molecules (COMs: CH_3OH , $^{13}\text{CH}_3\text{OH}$, CH_2DOH , and CH_3OCH_3) are detected. The molecular abundances relative to CH_3OH are similar to those of another outer Galactic hot core, demonstrating that chemically rich hot cores exist in different regions of the outer Galaxy. We also compared molecular abundances among hot cores in the inner Galaxy, outer Galaxy, and Magellanic Clouds. This comparison revealed that the metallicity-corrected $N(\text{SO}_2)/N(\text{H}_2)$ ratios of outer Galactic hot cores are significantly lower than those of the inner Galactic ones, while their $N(\text{CH}_3\text{OH})/N(\text{H}_2)$ ratios are similar. The Magellanic hot cores show different trends despite having metallicities similar to those of the outer Galaxy, indicating that the chemical complexity of hot cores is governed by environmental conditions (e.g., cosmic ray intensity and dust temperature) rather than simple metallicity scaling. These environmental differences would also affect the production efficiency of COMs derived from CH_3OH , as the $N(\text{CH}_3\text{OCH}_3)/N(\text{CH}_3\text{OH})$ and $N(\text{C}_2\text{H}_5\text{OH})/N(\text{CH}_3\text{OH})$ ratios in the outer Galactic sources are moderately lower than those of inner Galactic sources. The $N(\text{CH}_2\text{DOH})/N(\text{CH}_3\text{OH})$ ratio of Sh 2-283-1a SMM1 is $1.5^{+3.9\%}_{-1.2\%}$, comparable to that of inner Galactic high-mass sources.

Keywords: astrochemistry — ISM: molecules — stars: protostars — outer galaxy — radio lines: ISM

1. INTRODUCTION

The outer Galaxy, which is defined as having a galactocentric distance (D_{GC}) larger than ~ 13.5 kpc, where the gas surface density starts to drop (e.g., Wolfire et al. 2003; Sun et al. 2024), is an excellent laboratory for understanding the chemical complexity in different environments from the solar-neighborhood. This region

presents the distinctive physical properties, such as lower metallicity compared to the solar-neighborhood ($\lesssim 1/3 Z_{\odot}$; Fernández-Martín et al. 2017; Wenger et al. 2019) and lower gas density (Nakanishi & Sofue 2016). Moreover, perturbations from spiral arms and supernova explosions are expected to be minimal, as this region lies beyond the main arms of the Galaxy and exhibits a significantly low star formation rate (e.g., Reid et al. 2019; Elia et al. 2022). In addition, its proximity to the Sun allows us to investigate more compact structures in star-forming regions than in the other known low-metallicity environments, such as the Large Magellanic Cloud (LMC; $\sim 1/2\text{--}1/3 Z_{\odot}$) and the Small Magellanic Cloud (SMC; $\sim 1/5\text{--}1/10 Z_{\odot}$), which are located at distances of $\sim 50\text{--}60$ kpc (Pietrzyński et al. 2013; Graczyk et al. 2020).

Corresponding author: Toki Ikeda
 tokiikeda0122@gmail.com

Corresponding author: Takashi Shimonishi
 shimonishi@env.sc.niigata-u.ac.jp

A hot molecular core (hot core) represents one of the early phases in star formation, playing a pivotal role in the emergence and development of complex molecules in the interstellar medium (ISM). Hot cores are characterized by the presence of warm ($T \gtrsim 100$ K), dense ($n \gtrsim 10^6$ cm $^{-3}$), and compact (<0.1 pc) molecular gas associated with a central protostar (e.g., [van Dishoeck & Blake 1998](#); [Kurtz et al. 2000](#)). The chemically rich nature of hot cores is initiated by the sublimation of ice mantles formed on the dust surfaces. Before and during the heating of ice mantles by stellar radiation, grain surface reactions are thought to contribute to the formation of complex organic molecules (COMs: molecules consisting of at least six atoms) (e.g., [Garrod & Herbst 2006](#); [Herbst & van Dishoeck 2009](#)). These processes enrich gas-phase molecules, and consequently, various molecular species can be detected towards hot cores with radio and infrared observations via molecular transitions. Hence, the detailed study of hot core chemistry is crucial to unveil the chemical evolution in star-forming regions.

Recent ALMA (the Atacama Large Millimeter/submillimeter Array) observations have revealed the presence of hot cores in low-metallicity environments, such as the LMC and SMC ([Shimonishi et al. 2016, 2020, 2023, 2025](#); [Sewilo et al. 2018, 2022](#); [Hamedani Golshan et al. 2024](#); [Broadmeadow et al. 2025](#)), and the outer Galaxy at D_{GC} of 19.0 kpc ($\sim 1/4 Z_{\odot}$; [Shimonishi et al. 2021](#)). The comparison of molecular abundances among the Magellanic hot cores has suggested that there are large variations, especially for organic molecules. In some sources, organic molecules are significantly depleted beyond what would be expected from metallicity differences alone (see [Shimonishi 2024](#), and references therein). This large variation suggests that the molecular compositions of hot cores do not simply scale with the environmental metallicity, but are also strongly influenced by other factors, such as the degree of surrounding star-formation activity. On the other hand, detections of hot cores in the outer Galaxy have so far been limited, with only one source reported in [Shimonishi et al. \(2021\)](#). They have reported that the outer Galactic hot core, WB89-789 SMM1, shows a very similar organic molecular composition to its counterparts in the inner Galaxy. However, it remains unclear whether such molecular complexity is also present in other star-forming regions in the outer Galaxy. Although the outer Galaxy and the Magellanic Clouds share similar low-metallicity conditions, their environments are expected to differ significantly due to the differences in star formation activity. The Magellanic Clouds are characterized by active star formation, which presumably results in strong stellar feedback, such as high cosmic ray intensity and high dust temperature (e.g., [Shimonishi et al. 2016, 2020](#)). In contrast, the outer Galaxy is a relatively quiescent environment where such external influence would be much weaker. Since phar-

tochemistry and dust surface chemistry play a vital role in generating complex molecules in star-forming regions (e.g., [Herbst & van Dishoeck 2009](#), and references therein), comparing the chemical properties of hot cores in these regions allows us to investigate whether the chemical properties vary depending on environmental factors other than metallicity (e.g., cosmic ray intensity). Therefore, increasing the sample size of hot cores in the outer Galaxy is crucial for such comparative studies.

We conducted a protostellar survey toward the five outer Galactic star-forming regions (Sh 2-283, NOMF05-16, 19, 23, and 63; $D_{\text{GC}} = 15.7\text{--}17.4$ kpc) with ALMA. Detailed information about the survey, including target selection criteria, can be found in [Ikeda et al. \(2025\)](#). As a result of the survey, five protostellar objects associated with bipolar outflows were detected with CO($J = 3\text{--}2$) line emission, indicating that star formation is ongoing in these regions ([Ikeda et al. 2025](#)). Moreover, one of these outflow-driving sources, Sh 2-283-1a SMM1, showed a chemically rich nature, and a variety of molecular transition lines including high-excitation lines ($E_u > 100$ K) of CH₃OH and SO₂ were detected.

In this paper, we report the results of the detailed chemical analyses for this hot core located in the outer Galaxy. In Section 2, we describe the observation details and the data reduction. The observational results, including the observed molecular spectra and images, as well as analyses of the physical and chemical properties of the source, are given in Section 3. Discussions on the comparisons of the chemical properties of this source with the inner Galactic and Magellanic hot cores are presented in Section 4. The summary of this paper is given in Section 5.

2. OBSERVATIONS AND DATA REDUCTION

2.1. Sh 2-283-1a SMM1

The target source is located in the star-forming region Sh 2-283 in the outer Galaxy and is known to be associated with an H_{II} region ([Fich & Silkey 1991](#)). According to the astrometric data of a nearby cluster member (ALS 18674) in the Gaia Early Data Release 3 (Gaia source ID 3119827723711464576, [Gaia Collaboration et al. 2021](#); [Bragança et al. 2019](#)), the distance to the Sh 2-283 region is estimated to be $7.9^{+1.2}_{-1.1}$ kpc, which corresponds to the galactocentric distance of $15.7^{+1.1}_{-0.9}$ kpc ([Ikeda et al. 2025](#)). The metallicity of this region is estimated to be approximately 30% of the solar value based on optical spectroscopy of the associated H_{II} region ([Fernández-Martín et al. 2017](#)).

2.2. Observations

All data used in this work were obtained by ALMA as a part of the Cycle 9 program (2022.1.01270.S, PI: T. Shimonishi). The band 7 receiver was used to observe molecular emission lines (such as ¹²CO($J = 3\text{--}2$), HCO⁺($J = 4\text{--}3$),

$\text{SiO}(J = 8-7)$, SO , SO_2 , and CH_3OH) and 0.87 mm continuum. Five spectral windows (SPWs) of the correlator were used in the frequency division mode. The channel spacing for all SPWs was set to 976.6 kHz (corresponding to 0.85 km s^{-1} at 345 GHz). Two SPWs with a bandwidth of 0.938 GHz cover the sky frequencies of 344.038–344.976 and 344.978–345.916 GHz. The other three SPWs were set to cover the sky frequencies of 345.919–347.794, 346.169–358.044, and 356.961–358.836 GHz, in which the bandwidth was 1.875 GHz. Sh 2-283-1a SMM1 was observed in October 2022. The antenna configuration was C-2, resulting in a maximum baseline length of 313 m. The on-source time was 27.2 minutes. The observations were conducted in three execution blocks. During the observation period, 45 antennas were operated except for one observation block, in which 42 antennas were used. The bandpass calibrators were J0510+1800 and J0750+1231, and the phase calibrator was J0641-0320.

2.3. Data reduction

Data reduction, including calibration and imaging, was performed with the Common Astronomy Software Applications package (CASA: [CASA Team et al. 2022](#)) version 6.4.1.12. The raw data were calibrated with the pipeline script provided by the observatory for initial data flagging, the calibration of bandpass, complex gain, and flux scaling (pipeline version 2022.2.0.64). The visibilities of the line emissions were obtained by subtracting the continuum visibilities using the *uvcontsub* task in CASA. The clean images were produced using the *tclean* task in CASA. The line image cubes were obtained adopting Briggs weighting with a robust parameter of 0.5 for each SPW. In order to improve the signal-to-noise ratio, we performed phase self-calibration using the continuum after the calibration. One round of phase self-calibration was applied with a solution interval of 60 seconds. Finally, we corrected the primary beam patterns using the *impbcor* task. The systematic error on the absolute flux was approximately 10% according to the ALMA technical handbook¹.

The average beam size of the line images is $0''.79 \times 0''.68$, which corresponds to $6.2 \times 10^3 \text{ au} \times 5.4 \times 10^3 \text{ au}$ at the distance of Sh 2-283 (7.9 kpc from the Sun). The maximum recoverable scale is about $6''.3$ ($\sim 5.0 \times 10^4 \text{ au}$ at 7.9 kpc).

3. RESULTS AND ANALYSIS

3.1. Spectra

Figure 1 shows the submillimeter spectra extracted from the elliptical region ($0''.89 \times 0''.70$) centered at RA = $6^{\text{h}}38^{\text{m}}29.660$ and Dec = $0^{\circ}44'40''.75$ (ICRS), which corresponds to the emission peak of CH_3OH and the 0.87 mm

continuum. Spectral lines were identified by determining the systemic velocity (V_{sys}) as 53.2 km s^{-1} from the CH_3OH ($5_4 \text{A}^- - 6_3 \text{A}^-$) line, with the aid of the Cologne Database for Molecular Spectroscopy (CDMS, [Müller et al. 2001, 2005](#)) and the Jet Propulsion Laboratory (JPL, [Pickett et al. 1998](#)). The detection criteria adopted here were a 3σ significance level and the velocity coincidence of the line emission with V_{sys} of the target ($\sim \pm 2 \text{ km s}^{-1}$ from V_{sys}). For the lines whose significance level was higher than 2.5σ but lower than 3σ and the emission distribution coincides with the continuum peak, we regarded them as tentative detections. We derived the line parameters (the peak brightness temperature, FWHM, LSR velocity, and integrated intensity) by fitting a Gaussian profile to each detected line (colored lines in Figure 1). For some weak lines, two channels were binned, or the Savitzky-Golay filter (window size of 5 channels and polynomial order of 3) was used to reduce noise. The line parameters for the detected molecular lines are summarized in Table 1. The detailed fitting results are summarized in Appendix A.

As shown in Figure 1, we detected a variety of molecular species such as CO , SO , SO^+ , SO_2 , HCO^+ , H^{13}CO^+ , SiO , H^{13}CN , HC^{15}N , D_2CO , *trans*- HCOOH , CH_3OH , $^{13}\text{CH}_3\text{OH}$, CH_2DOH , and CH_3OCH_3 toward Sh 2-283-1a SMM1. For SO_2 , CH_3OH , and CH_2DOH , multiple high excitation lines with different upper state energies were detected. We also tentatively detected NS , H_2CCO , HC_3N , and CH_3SH . Although CH_3SH ($14_{1,13,1} - 13_{1,12,1}$) was detected with a signal above 3σ of the rms noise level (see Table 1), the other CH_3SH line ($14_{1,13,0} - 13_{1,12,0}$), which has a similar upper state energy and line intensity ($E_u = 133.8 \text{ K}$), remained undetected. We thus regard the CH_3SH detection as tentative.

The typical measured line widths are 3–6 km s^{-1} . Although most of the molecular lines show a single velocity component peaked near V_{sys} , CO has multiple velocity components because it traces protostellar outflows and jets ([Ikeda et al. 2025](#)). Note that the derived intensities of the lines associated with broad wing components (e.g., SO and HCO^+) may be slightly overestimated due to the contamination from the broad components.

3.2. Images

Figure 2 shows the integrated intensity maps of the detected molecular species. The images were generated by integrating the spectral data in the velocity range where the emission is detected. The integration range (typically $\sim \pm \text{FWHM}$) was determined by visual inspection for each line to ensure that broad wing components were included.

For SO , SO_2 , *trans*- HCOOH , CH_3OH , CH_2DOH , and CH_3OCH_3 , several lines were stacked to reduce the noise level. Contours and color in this figure show the 0.87 mm continuum and each molecular emission, respectively.

¹ <https://almascience.nao.ac.jp/documents-and-tools/cycle11/alma-technical-handbook>

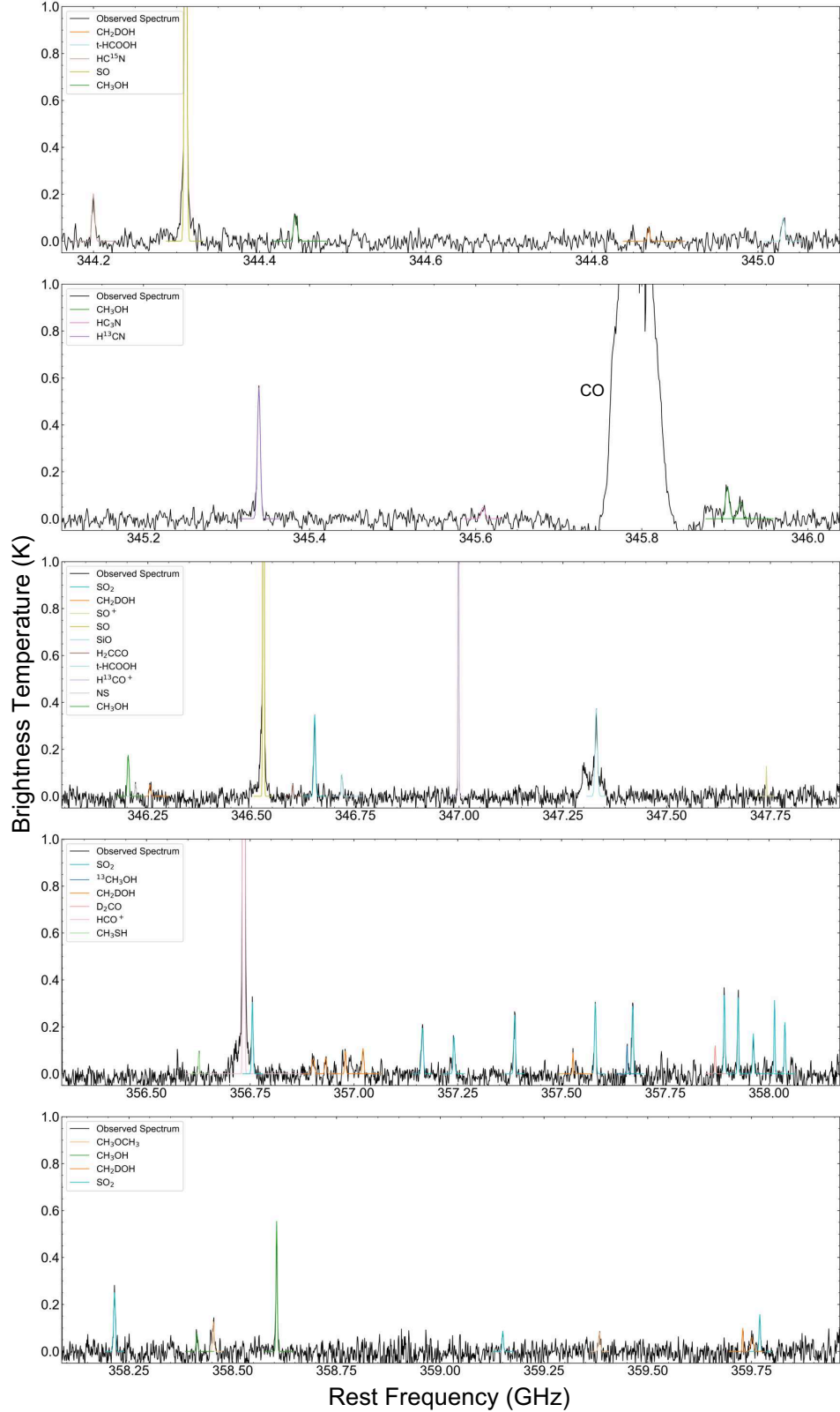


Figure 1. ALMA Band 7 spectra of Sh 2-283-1a SMM1 extracted from the elliptical region ($0.^{\circ}89 \times 0.^{\circ}70$) centered at RA = $6^{\text{h}}38^{\text{m}}29\text{.}660$ and Dec = $0^{\circ}44'40\text{.}'75$ (ICRS), which corresponds to the emission peak of the 0.87 mm continuum and molecular emissions. The lines with different colors represent the results of Gaussian fitting for each molecular line (Table 1). The systemic velocity of 53.2 km s^{-1} is assumed to identify the molecular lines.

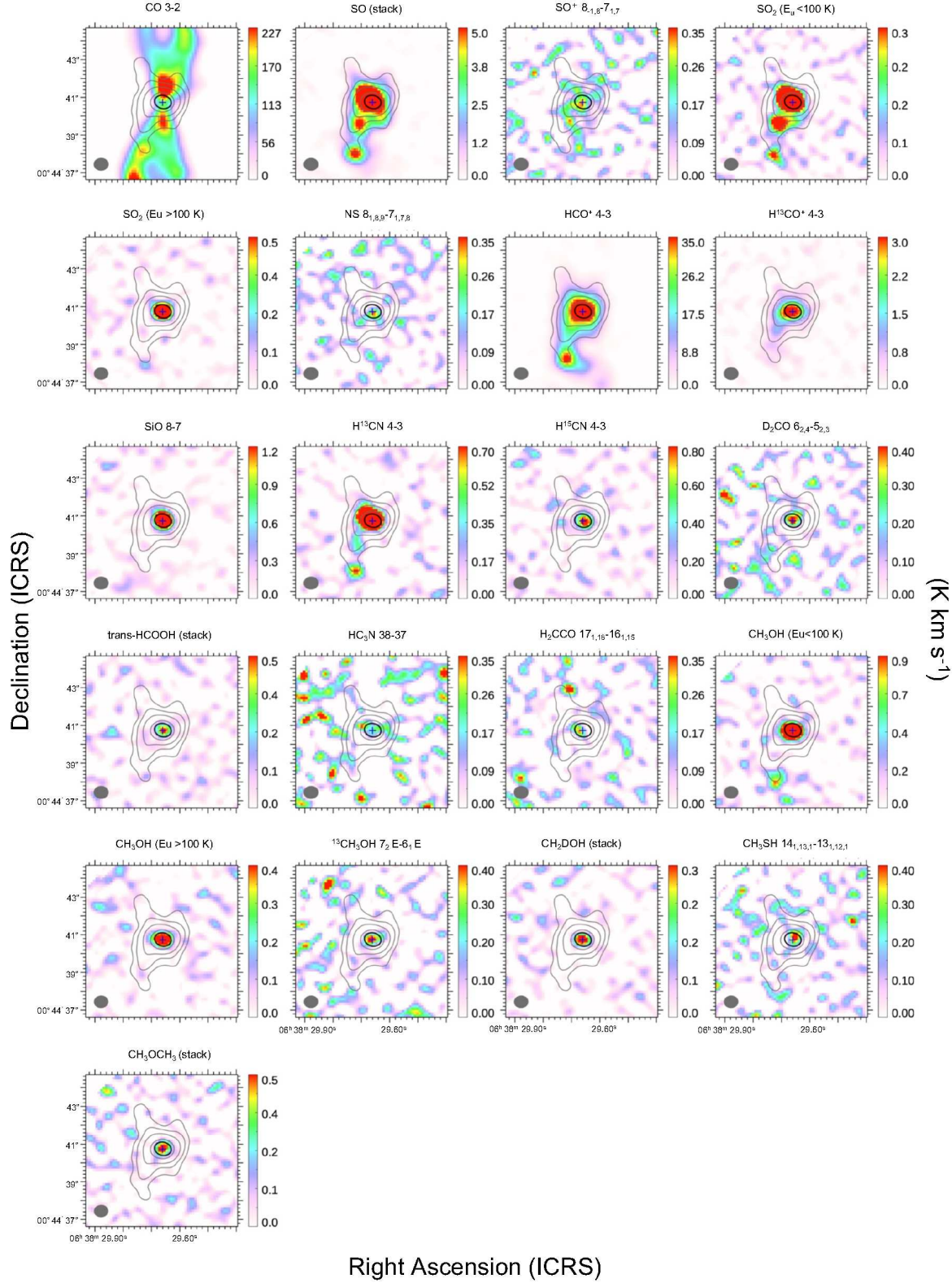


Figure 2. The integrated intensity maps of the detected molecular lines. Grey contours show the emission distribution of 0.87 mm continuum, and the contour levels are 5σ , 15σ , 25σ , and 100σ of the rms noise level ($1\sigma = 0.07$ mJy beam $^{-1}$). The blue cross indicates the peak position of 0.87 mm continuum. The black open circle represents the extraction region of the spectra used for the discussion in the text. For molecular species with multiple line detections, lines are stacked in order to reduce the noise level. The synthesized beam size is shown in the bottom left corner, as a gray ellipse.

Most molecular emissions have their intensity peaks near the 0.87 mm continuum peak. CO is extended in a north-south direction from the continuum peak, and it traces the protostellar outflows and jets as discussed in Ikeda et al. (2025). The emission distributions of SO, SO₂ ($E_u < 100$ K), HCO⁺, H¹³CN⁺, and CH₃OH ($E_u < 100$ K) are extended compared to higher- E_u lines, and these lines have the secondary peak on the south side from the continuum peak (Figure 2).

3.3. Column densities and gas temperatures

Since we detected multiple rotational transitions with different excitation energies for SO₂, CH₃OH, and CH₂DOH, we conducted the rotational diagram analysis to estimate the rotational temperatures and column densities of these molecules. Here, we assume that the molecular emissions are optically thin and under the condition of the local thermodynamic equilibrium (LTE). The derived gas density of Sh 2-283-1a SMM1 is $\sim 4 \times 10^6$ cm⁻³ (Section 3.4), which is a typical value for hot cores (e.g., van Dishoeck & Blake 1998; Kurtz et al. 2000). Shimonishi et al. (2021) demonstrated that column densities derived from LTE analysis are generally consistent with those from non-LTE analysis within a factor of two for the source with spatial resolution (~ 5000 au) and gas density comparable to those in this work. Thus, we consider the LTE assumption to be reasonable for this source.

We use the following formula to perform the rotational diagram analysis in the standard way (e.g., Sutton et al. 1995; Goldsmith & Langer 1999):

$$\log\left(\frac{N_u}{g_u}\right) = -\left(\frac{\log e}{T_{\text{rot}}}\right)\left(\frac{E_u}{k}\right) + \log\left(\frac{N}{Q(T_{\text{rot}})}\right), \quad (1)$$

where

$$\frac{N_u}{g_u} = \frac{3k \int T_b dV}{8\pi^3 \nu S \mu^2}, \quad (2)$$

and N_u is the column density of the molecules, k is the Boltzmann constant, T_b is the brightness temperature, g_u is the degeneracy of the upper state, T_{rot} is the rotational temperature, $Q(T_{\text{rot}})$ is the partition function at T_{rot} , ν is the rest frequency, S is the line strength, μ is the dipole moment, and E_u is the upper state energy. All the spectroscopic parameters ($Q(T_{\text{rot}})$, g_u , ν , μ , E_u , and S) are extracted from the CDMS or JPL database.

In the fitting processes, SO₂($J = 13_{2,12}-12_{1,11}$) was removed from the fitting since this line was significantly blended with H¹³CN($J = 4-3$). For CH₂DOH, we used the a-type ($\Delta K_a = 0$ and $K_c = 1$) R-branch ($\Delta J = 1$) transitions. While CH₃OH and CH₂DOH were fitted by a single temperature component, SO₂ seemed to have multiple temperature components. We separated the straight-line fit for SO₂ at E_u

< 100 K and $E_u \geq 100$ K. For the molecular abundance comparisons discussed in Section 4.2, we use the SO₂ column density constrained from the lines with $E_u \geq 100$ K. The results of the rotational diagram analysis are shown in Figure 3.

For molecular species where only a single (or two) lines have been detected and rotational diagram analysis could not be performed, we calculated the column densities by solving Equation 1 for N assuming the rotational temperatures. Based on the results of the rotational diagram analysis, we adopted rotational temperatures of 50 K and 150 K for the cold and warm gas components, respectively. Molecular species with $E_u \lesssim 100$ K and extended emission distributions around the continuum peak were assigned to the cold gas component tracing the relatively low-temperature region associated with a hot core ($T_{\text{rot}} = 50$ K). Specifically, we assumed that SO, SO⁺, NS, HCO⁺, H¹³CO⁺, SiO, H¹³CN, HC¹⁵N, and D₂CO trace the cold gas component. In contrast, molecular species with $E_u \gtrsim 100$ K and compact emission distributions (*trans*-HCOOH, HC₃N, H₂CCO, ¹³CH₃OH, CH₃SH, and CH₃OCH₃) were assumed to reside in the warm gas component associated with the hot core ($T_{\text{rot}} = 150$ K). The uncertainties of the derived column densities were calculated by combining the fitting errors (corresponding to the 2σ level) and the 10% absolute flux uncertainty in quadrature. The derived column densities are summarized in Table 2.

The derived $N(\text{CH}_3\text{OH})/N(^{13}\text{CH}_3\text{OH})$ ratio for Sh 2-283-1a SMM1 is ~ 10 , which is significantly lower than the local ¹²C/¹³C ratio expected from the relation between the galactocentric distance and ¹²C/¹³C ratio ($\sim 80-120$ at 15.7 kpc; Yan et al. 2023). Although the line shapes of CH₃OH do not exhibit obvious signs of high optical thickness (see Appendix A), the emission is likely affected by optical thickness, leading to an underestimation of the column density derived from the rotational diagram analysis. To avoid this underestimation, we estimated $N(\text{CH}_3\text{OH})$ from the ¹³CH₃OH column density, assuming a ¹²C/¹³C ratio of 100 based on the isotope ratio gradients reported by Milam et al. (2005) and Yan et al. (2023) at $D_{\text{GC}} = 15.7$ kpc. The resulting $N(\text{CH}_3\text{OH})$ is 1.4×10^{16} cm⁻², which is approximately one order of magnitude higher than the value obtained from the rotational diagram analysis (Figure 3). We use this corrected value of $N(\text{CH}_3\text{OH}) = 1.4 \times 10^{16}$ cm⁻² in the discussion of molecular abundances. Note that we cannot rule out the possibility that this value is overestimated due to the uncertainties in the assumed ¹²C/¹³C ratio and rotational temperature.

3.4. Column density of molecular hydrogen

Table 1. Line Parameters

Molecule	Transition	E_u	Frequency	T_b	ΔV	$\int T_b dV$	V_{LSR}	RMS	Note
		(K)	(GHz)	(K)	(km s $^{-1}$)	(K km s $^{-1}$)	(km s $^{-1}$)	(K)	
CO	3–2	33	345.79599	~16	...	~157	...	0.02	...
SO	$N_J = 8_8-7_7$	87	344.31061	2.82 ± 0.04	2.6	7.88 ± 0.12	53.0	0.02	...
SO	$N_J = 8_9-7_8$	79	346.52848	4.26 ± 0.04	2.5	11.41 ± 0.12	53.1	0.02	...
SO $^+$	$8_{-1,8}-7_{1,7}$	70	347.74001	0.13 ± 0.05	1.6	0.21 ± 0.08	52.9	0.02	...
SO $_2$	$4_{4,0}-4_{3,1}$	48	358.03789	0.22 ± 0.04	2.8	0.68 ± 0.16	53.0	0.03	...
SO $_2$	$5_{4,2}-5_{3,3}$	53	358.01315	0.32 ± 0.05	2.4	0.80 ± 0.14	53.2	0.03	...
SO $_2$	$6_{4,2}-6_{3,3}$	59	357.92585	0.34 ± 0.04	2.8	1.04 ± 0.15	53.4	0.03	...
SO $_2$	$7_{4,4}-7_{3,5}$	65	357.89244	0.35 ± 0.04	3.1	1.16 ± 0.15	53.3	0.03	...
SO $_2$	$8_{4,4}-8_{3,5}$	72	357.58145	0.30 ± 0.04	3.7	1.19 ± 0.17	53.4	0.03	...
SO $_2$	$9_{4,6}-9_{3,7}$	81	357.67182	0.29 ± 0.04	3.8	1.18 ± 0.16	53.5	0.03	...
SO $_2$	$10_{4,6}-10_{3,7}$	90	356.75519	0.31 ± 0.04	3.5	1.13 ± 0.14	53.2	0.03	(1)
SO $_2$	$11_{4,8}-11_{3,9}$	100	357.38758	0.25 ± 0.04	3.9	1.04 ± 0.16	53.6	0.03	...
SO $_2$	$13_{2,12}-12_{1,11}$	93	345.33854	0.56 ± 0.03	3.7	2.19 ± 0.12	52.9	0.02	(2)
SO $_2$	$13_{4,10}-13_{3,11}$	123	357.16539	0.20 ± 0.04	4.8	1.01 ± 0.18	53.7	0.03	...
SO $_2$	$15_{4,12}-15_{3,13}$	150	357.24119	0.16 ± 0.04	3.9	0.67 ± 0.15	53.5	0.03	...
SO $_2$	$17_{4,14}-17_{3,15}$	180	357.96290	0.17 ± 0.04	3.3	0.60 ± 0.16	53.9	0.03	...
SO $_2$	$19_{1,19}-18_{0,18}$	168	346.65217	0.35 ± 0.03	4.3	1.61 ± 0.14	53.4	0.02	...
SO $_2$	$19_{4,16}-19_{3,17}$	214	359.77068	0.16 ± 0.04	3.2	0.54 ± 0.15	53.8	0.03	...
SO $_2$	$20_{0,20}-19_{1,19}$	185	358.21563	0.25 ± 0.04	4.1	1.09 ± 0.16	53.5	0.03	...
SO $_2$	$25_{3,23}-25_{2,24}$	321	359.15116	0.09 ± 0.04	3.1	0.28 ± 0.14	53.5	0.03	...
NS	$8_{1,8,9}-7_{-1,7,8}$	70	346.22014	0.05 ± 0.03	3.5	0.20 ± 0.10	52.9	0.02	^(a) (3)
SiO	8–7	75	347.33058	0.38 ± 0.03	5.9	2.36 ± 0.15	53.3	0.02	...
HCO $^+$	4–3	43	356.73422	18.30 ± 0.05	2.7	52.99 ± 0.20	53.0	0.03	...
H 13 CO $^+$	4–3	42	346.99834	1.49 ± 0.04	2.1	3.26 ± 0.13	53.1	0.02	...
H 13 CN	4–3	41	345.33977	0.56 ± 0.03	3.7	2.19 ± 0.12	54.0	0.02	...
HC 15 N	4–3	41	344.20011	0.20 ± 0.03	3.2	0.69 ± 0.12	53.5	0.02	...
D $_2$ CO	$6_{2,4}-5_{2,3}$	81	357.87145	0.12 ± 0.05	2.5	0.32 ± 0.14	54.2	0.03	...
trans-HCOOH	$16_{0,16}-15_{0,15}$	143	345.03056	0.10 ± 0.03	4.0	0.43 ± 0.12	53.2	0.02	...
trans-HCOOH	$15_{2,13}-14_{2,12}$	144	346.71886	0.09 ± 0.03	3.5	0.35 ± 0.12	54.3	0.02	...
HC $_3$ N	38–37	323	345.60901	0.05 ± 0.03	4.2	0.24 ± 0.15	53.1	0.02	^(a) (b)
H $_2$ CCO	$17_{1,16}-16_{1,15}$	163	346.60045	0.05 ± 0.04	2.5	0.14 ± 0.10	54.3	0.02	^(a)
CH $_3$ OH	4 ₁ E–3 ₀ E	44	358.60580	0.55 ± 0.04	3.0	1.76 ± 0.15	53.1	0.03	...
CH $_3$ OH	$5_{4,A^-}-6_{3,A^-}$	115	346.20272	0.17 ± 0.03	4.2	0.79 ± 0.13	53.2	0.02	(4)
CH $_3$ OH	$10_{6,E}-11_{5,E}$	306	358.41465	0.08 ± 0.04	3.5	0.30 ± 0.15	54.0	0.03	(c)
CH $_3$ OH	$16_{1,A^-}-15_{2,A^-}$	333	345.90392	0.14 ± 0.03	4.9	0.72 ± 0.14	54.0	0.02	(c)
CH $_3$ OH	$18_{-3,E}-17_{-4,E}$	459	345.91926	0.07 ± 0.03	6.0	0.45 ± 0.14	53.5	0.02	(c)
CH $_3$ OH	$19_{1,A^+}-18_{2,A^+}$	451	344.44343	0.11 ± 0.03	4.2	0.50 ± 0.13	53.5	0.02	(c)
13 CH $_3$ OH	$7_2 E-6_1 E$	86	357.65795	0.13 ± 0.05	2.2	0.30 ± 0.12	53.2	0.03	...
CH $_2$ DOH	$2_{1,1}e_1-2_{0,2}e_0$	23	344.86895	0.06 ± 0.04	2.8	0.17 ± 0.10	53.7	0.02	^(a) (c)
CH $_2$ DOH	$3_{1,2}e_1-3_{0,3}e_0$	29	346.25650	0.05 ± 0.03	3.8	0.21 ± 0.16	54.1	0.02	^(a) (c)
CH $_2$ DOH	$7_{1,6}e_1-7_{0,7}e_0$	77	357.52856	0.09 ± 0.05	2.1	0.21 ± 0.13	54.1	0.03	(c)
CH $_2$ DOH	$8_{0,8}o_1-7_{0,7}o_1$	95	356.98158	0.10 ± 0.05	3.2	0.34 ± 0.13	55.2	0.03	(5)
CH $_2$ DOH	$8_{1,7}e_2-7_{1,6}e_2$	101	359.75351	0.06 ± 0.03	5.7	0.38 ± 0.17	55.0	0.02	(b)
CH $_2$ DOH	$8_{2,6}e_0-7_{2,5}e_0$	94	359.72880	0.10 ± 0.05	2.3	0.25 ± 0.14	53.2	0.03	...
CH $_2$ DOH	$8_{2,7}e_1-7_{2,6}e_1$	104	356.89967	0.07 ± 0.03	5.9	0.41 ± 0.18	51.5	0.02	^(b) (6)
CH $_2$ DOH	$8_{3,6}e_2-7_{3,5}e_2$	132	357.02078	0.11 ± 0.04	4.0	0.46 ± 0.15	52.4	0.03	(7)
CH $_2$ DOH	$8_{4,4}e_1-7_{4,3}e_1$	149	356.93241	0.07 ± 0.04	3.7	0.30 ± 0.17	53.5	0.03	^(b) (8)
CH $_3$ SH	$14_{1,13,1}-13_{1,12,1}$	134	356.62701	0.10 ± 0.05	2.7	0.28 ± 0.15	53.8	0.03	^(a)
CH $_3$ OCH $_3$	$5_{5,0}-4_{4,0}$ EE	49	358.45202	0.13 ± 0.04	3.9	0.52 ± 0.14	52.0	0.03	(9)
CH $_3$ OCH $_3$	$12_{3,10}-11_{2,9}$ EE	84	359.38459	0.08 ± 0.03	4.4	0.39 ± 0.15	54.1	0.02	^(b) (10)

NOTE—The uncertainties of the line parameters are at the 2σ level derived from Gaussian fitting. ^(a)Tentative detection. ^(b)Two channels were binned to reduce noise. ^(c)The Savitzky-Golay filter was applied to reduce noise. (1) Partially blend with HCO $^+$ (4–3). (2) Blend with SO $_2$ (13_{2,12}–12_{1,11}). (3) Blended with three hyperfine components. (4) Blended with two hyperfine components. (5) Blended with five hyperfine components. (6) Blended with three hyperfine components. (7) Blended with two hyperfine components. (8) Blended with two hyperfine components. (9) Blended with six hyperfine components. (10) Blended with four hyperfine components.

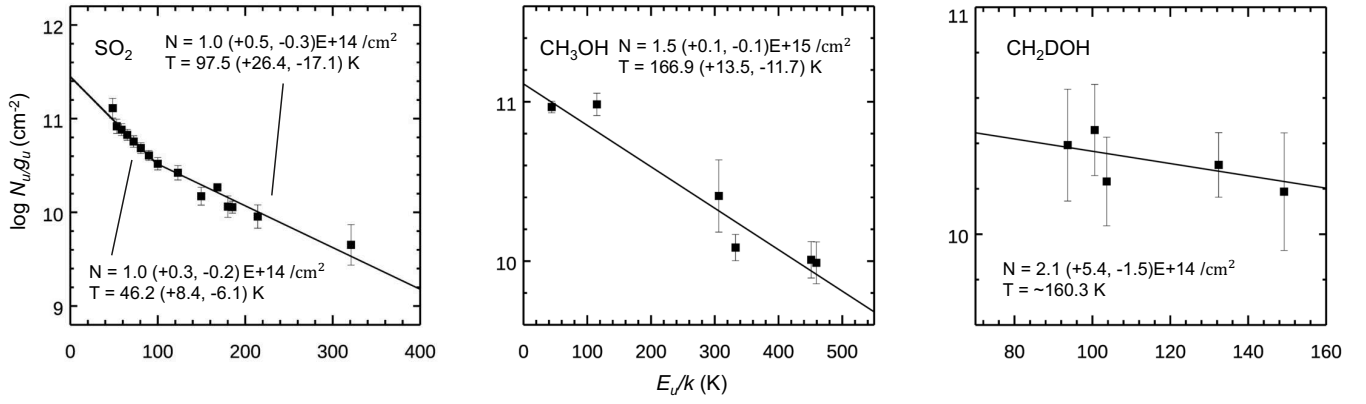


Figure 3. The results of the rotational diagram analysis for SO₂, CH₃OH, and CH₂DOH. The solid lines indicate the results of the linear regression. The derived column densities and rotational temperatures are shown in each panel. For SO₂, the left line is fitted with using the transitional lines with $E_u < 100$ K, while the right solid line is fitted with using the transitional lines with $E_u \geq 100$ K. SO₂(13_{2,12}–12_{1,11}) is removed in the fitting since this line is significantly blended with H¹³CN (4–3). See Section 3.3 for the details.

The column density of molecular hydrogen (N_{H_2}) is estimated using the dust continuum data. We used the following formula based on the standard treatment of optically thin dust emission:

$$N_{\text{H}_2} = \frac{F_{\nu}/\Omega}{2\kappa_{\nu}B_{\nu}(T_{\text{d}})Z\mu m_{\text{H}}}, \quad (3)$$

and F_{ν}/Ω is the continuum flux density per beam solid angle as estimated from the observations, and κ_{ν} is the mass absorption coefficient of dust grains coated by thin ice mantles taken from [Ossenkopf & Henning \(1994\)](#) and we use $1.89 \text{ cm}^2 \text{ g}^{-1}$ at $870 \mu\text{m}$. T_{d} is the dust temperature, $B_{\nu}(T_{\text{d}})$ is the Planck function at $T = T_{\text{d}}$, Z is the dust-to-gas mass ratio, μ is the mean atomic mass per hydrogen (1.41; [Cox 2000](#)), and m_{H} is the hydrogen mass. We used the dust-to-gas mass ratio of 0.0024, derived by scaling the canonical local ISM value of 0.008 with the metallicity of the target ($\sim 0.3 Z_{\odot}$). The uncertainty in the dust temperature introduces uncertainty in the derivation of N_{H_2} . We assumed the dust temperature to be equal to that of the high-temperature molecular gas component (150 K), based on the results of the rotational diagram analysis (Section 3.3). The derived N_{H_2} is $1.4 \times 10^{23} \text{ cm}^{-2}$, with a range of $(1.1\text{--}2.7) \times 10^{23} \text{ cm}^{-2}$ for dust temperatures of 80–180 K based on the T_{rot} of SO_2 and CH_3OH (Figure 3). Assuming non-ice dust, the derived N_{H_2} is $7.4 \times 10^{22} \text{ cm}^{-2}$ with $\kappa_{\nu} = 3.54 \text{ cm}^2 \text{ g}^{-1}$ at $870 \mu\text{m}$ and $T_{\text{d}} = 150 \text{ K}$. In this paper, we adopt $N_{\text{H}_2} = 1.4^{+1.3}_{-0.3} \times 10^{23} \text{ cm}^{-2}$ as the representative value of H_2 column density. The gas density of the core was estimated by dividing the N_{H_2} by its extent ($6.5 \times 10^3 \text{ au}$ is assumed), and the derived value is $3.7 \times 10^6 \text{ cm}^{-3}$.

After determining N_{H_2} , we derived the fractional abundances of the detected molecular species. The derived molecular abundances are summarized in Table 2. The uncertainties for the abundance ratios used in Section 4 were calculated using standard error propagation rules.

4. DISCUSSION

4.1. Hot molecular core associated with Sh 2-283-1a SMM1

Sh 2-283-1a SMM1 exhibits (1) a compact distribution of envelope gas ($\sim 0.03 \text{ pc}$, Section 3.1), (2) a high gas temperature ($> 100 \text{ K}$, Section 3.3), (3) a high gas density ($\sim 4 \times 10^6 \text{ cm}^{-3}$, Section 3.4), and (4) the detection of various molecular species, including COMs. These characteristics suggest that this source is associated with a hot core. The luminosity of Sh 2-283-1a SMM1 is estimated to be $10^3\text{--}10^4 \text{ L}_{\odot}$ ([Ikeda et al. 2025](#)), suggesting that it hosts an intermediate- or high-mass protostar.

4.2. Chemical properties of the outer Galactic hot cores

Figure 4 compares the molecular abundances normalized by $N(\text{CH}_3\text{OH})$ between Sh 2-283-1a SMM1 and WB89-789 SMM1. The latter is the only previously reported hot

Table 2. Estimated Rotational Temperatures, Column Densities, and Fractional Abundances

Molecule	T_{rot}	$N(\text{X})$	$N(\text{X})/N(\text{H}_2)$
	(K)	(cm^{-2})	
H_2	–	$(1.4^{+1.3}_{-0.3}) \times 10^{23}$ ^(a)	–
SO	50	$(1.5 \pm 0.2) \times 10^{14}$	1.1×10^{-10}
SO^+	50	$(5.2 \pm 2.0) \times 10^{12}$	3.8×10^{-11}
SO_2	$46.2^{+8.4}_{-6.1}$	$(1.0^{+0.3}_{-0.2}) \times 10^{14}$	7.3×10^{-10}
	$97.5^{+26.4}_{-17.1}$	$(1.0^{+0.5}_{-0.3}) \times 10^{14}$	7.3×10^{-10}
NS	50	$(1.5 \pm 0.8) \times 10^{12}$	1.1×10^{-11}
HCO^+	50	$(2.3 \pm 0.2) \times 10^{13}$	1.7×10^{-10}
H^{13}CO^+	50	$(1.5 \pm 0.2) \times 10^{12}$	1.1×10^{-11}
SiO	50	$(3.2 \pm 0.4) \times 10^{12}$	2.3×10^{-11}
H^{13}CN	50	$(1.7 \pm 0.2) \times 10^{12}$	1.2×10^{-11}
HC^{15}N	50	$(5.3 \pm 1.0) \times 10^{11}$	3.9×10^{-12}
D_2CO	50	$(3.4 \pm 1.6) \times 10^{12}$	2.5×10^{-11}
trans-HCOOH	150	$(4.7 \pm 1.7) \times 10^{13}$	3.4×10^{-10}
HC_3N	150	$(1.3 \pm 0.8) \times 10^{12}$	9.6×10^{-12}
H_2CCO	150	$(7.3 \pm 5.4) \times 10^{12}$	5.3×10^{-11}
CH_3OH	$166.9^{+13.5}_{-11.7}$	$(1.5^{+0.1}_{-0.1}) \times 10^{15}$	1.1×10^{-8}
	150 ^(b)	$(1.4 \pm 0.6) \times 10^{16}$	1.0×10^{-7}
$^{13}\text{CH}_3\text{OH}$	150	$(1.4 \pm 0.6) \times 10^{14}$	1.0×10^{-9}
CH_2DOH	~ 160	$(2.1^{+5.4}_{-1.5}) \times 10^{14}$	1.5×10^{-9}
CH_3SH	150	$(7.9 \pm 4.4) \times 10^{13}$	5.8×10^{-10}
CH_3OCH_3	150	$(2.0 \pm 0.6) \times 10^{14}$	1.5×10^{-9}

NOTE—The uncertainties of the column densities were calculated by combining the fitting errors (corresponding to the 2σ level) and the 10% absolute flux uncertainty in quadrature. ^(a)The uncertainty corresponds to the range of $N(\text{H}_2)$ derived assuming the dust temperatures of 80–180 K, consistent with the rotational temperatures of SO_2 and CH_3OH . ^(b)The column density of CH_3OH used for the abundance comparisons derived from that of $^{13}\text{CH}_3\text{OH}$ by scaling the $^{12}\text{C}/^{13}\text{C}$ ratio (assuming $^{12}\text{C}/^{13}\text{C} = 100$).

core in the outer Galaxy ($D_{\text{GC}} = 19.0 \text{ kpc}$; [Shimonishi et al. 2021](#)). Since CH_3OH lines with $E_{\text{u}} \geq 100 \text{ K}$ usually trace the hot gas arising from a high-temperature region where products of grain surface chemistry (e.g., COMs) are sublimated from dust mantles, such a comparison is useful for evaluating the chemical properties of hot cores ([Herbst & van Dishoeck 2009](#)). Moreover, we can mitigate the effect of metallicity differences by normalizing with CH_3OH .

In this figure, we compare the molecular abundances for 7 molecular species detected in both sources: two COMs (CH_2DOH and CH_3OCH_3 ; red), four organic molecules (trans-HCOOH , HC_3N , H_2CCO , and D_2CO ; blue), and SO_2 (green). Note that HC_3N and H_2CCO are tentatively detected in Sh 2-283-1a SMM1. Although the molecular abundances normalized by CH_3OH are overall higher in Sh 2-283-1a SMM1 by roughly a factor of two, these two outer Galactic hot cores share a similar chemical composition. This

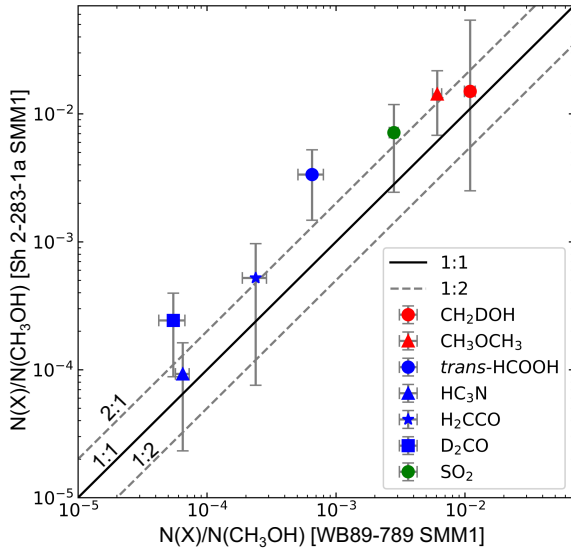


Figure 4. Comparison of the molecular abundances normalized by CH_3OH column density between the outer Galactic hot cores. The dotted lines represent the abundance ratio of 2:1 and 1:2 for Sh 2-283-1a SMM1, while the solid line represents that of 1:1. The molecular abundances of WB89-789 SMM1 are taken from Shimonishi et al. (2021).

indicates that Sh 2-283-1a SMM1 exhibits chemical complexity comparable to that of WB89-789 SMM1 reported by Shimonishi et al. (2021), which is located in a different region of the outer Galaxy.

4.3. Molecular abundances: Comparison with the Galactic and Magellanic hot cores

Figure 5 compares the molecular abundances of hot cores (CH_3OH and SO_2) relative to H_2 as a function of luminosity. The CH_3OH and SO_2 column densities for the inner Galactic sources were taken from Fuente et al. (2014); van Gelder et al. (2022a); Qin et al. (2022); Li et al. (2025) and Fuente et al. (2014); Santos et al. (2024). These sources have D_{GC} ranging from $\sim 0.2\text{--}8$ kpc (Appendix B). We calculated the H_2 column densities for the sources in Santos et al. (2024) by using the continuum data summarized in van Gelder et al. (2022a), following the method used in Section 3.4. We assumed the dust temperature is equal to the CH_3OH excitation temperature reported in van Gelder et al. (2022b).

The column densities of CH_3OH and SO_2 for the outer Galactic and Magellanic sources are obtained from the literature (Shimonishi et al. 2016, 2020, 2021, 2023, 2025; Sewilo et al. 2022; Hamedani Golshan et al. 2024; Broadmeadow et al. 2025). For some sources where H_2 column densities were originally derived assuming $T_{\text{dust}} < 100$ K, we recalculated them assuming that the dust temperature

is equal to the rotational temperature of either CH_3OH or SO_2 .

Figure 5(a) shows a comparison of the $N(\text{CH}_3\text{OH})/N(\text{H}_2)$ ratios among the sources described above. This figure demonstrates that the $N(\text{CH}_3\text{OH})/N(\text{H}_2)$ ratios vary significantly among the sources, and the abundances exhibit a large scatter, spanning approximately two orders of magnitude, even when limited to the inner Galactic sources. No correlation is found between the $N(\text{CH}_3\text{OH})/N(\text{H}_2)$ ratios and luminosity. The $N(\text{CH}_3\text{OH})/N(\text{H}_2)$ ratios of the outer Galactic sources are mutually similar, and the values can be approximately scaled with their metallicities when compared to the inner Galactic sources ($\sim 1/4$ of the median of the inner Galactic sources). However, for the Magellanic sources, the values are lower or, at best, lie near the lower limit of the inner Galactic sources, even when the values are corrected for their metallicities; the median values of abundances are only $\sim 1/27$ (LMC) and $\sim 1/90$ (SMC) of that of the inner Galactic sources.

Figure 6 shows the $N(\text{CH}_3\text{OH})/N(\text{H}_2)$ ratios as a function of T_{rot} of CH_3OH . In this figure, for the inner Galactic sources for which rotational temperatures of CH_3OH were not derived, the rotational temperatures of other COMs are used. For the LMC and SMC sources for which rotational temperatures of CH_3OH were not derived, the rotational temperatures of SO_2 are used. This figure indicates no correlation between the $N(\text{CH}_3\text{OH})/N(\text{H}_2)$ ratios and gas temperatures, suggesting that the $N(\text{CH}_3\text{OH})/N(\text{H}_2)$ ratio is independent of the current physical conditions of the sources. It is widely accepted that CH_3OH in hot cores is mainly formed on dust grain surfaces during the initial ice-forming stages via successive hydrogenation of CO , and as star formation proceeds, it is released into the gas phase via thermal desorption (e.g., Watanabe & Kouchi 2002). The formation efficiency of CH_3OH is significantly affected by the surrounding environment during these initial ice-forming stages, particularly by dust temperature. Since dust temperatures of $\lesssim 20$ K are required for CO depletion onto dust grain surfaces and to maintain hydrogen atoms in the solid phase, such a low-temperature environment is essential for the efficient formation of CH_3OH in protostellar regions. These points suggest that the Magellanic sources, especially their CH_3OH -poor sources, likely experienced environments different from the Galactic ones, thereby affecting the formation efficiency of CH_3OH . Shimonishi et al. (2020) conducted astrochemical simulations to explain the low abundance of CH_3OH in LMC hot cores, finding that the CH_3OH abundance in a hot core significantly decreases as the visual extinction during the ice-forming stage decreases (see their Figure 9). This is likely due to the inhibition of hydrogenation reactions of CO under high dust temperatures, and this effect is particularly enhanced in the LMC, where active star formation is ongoing

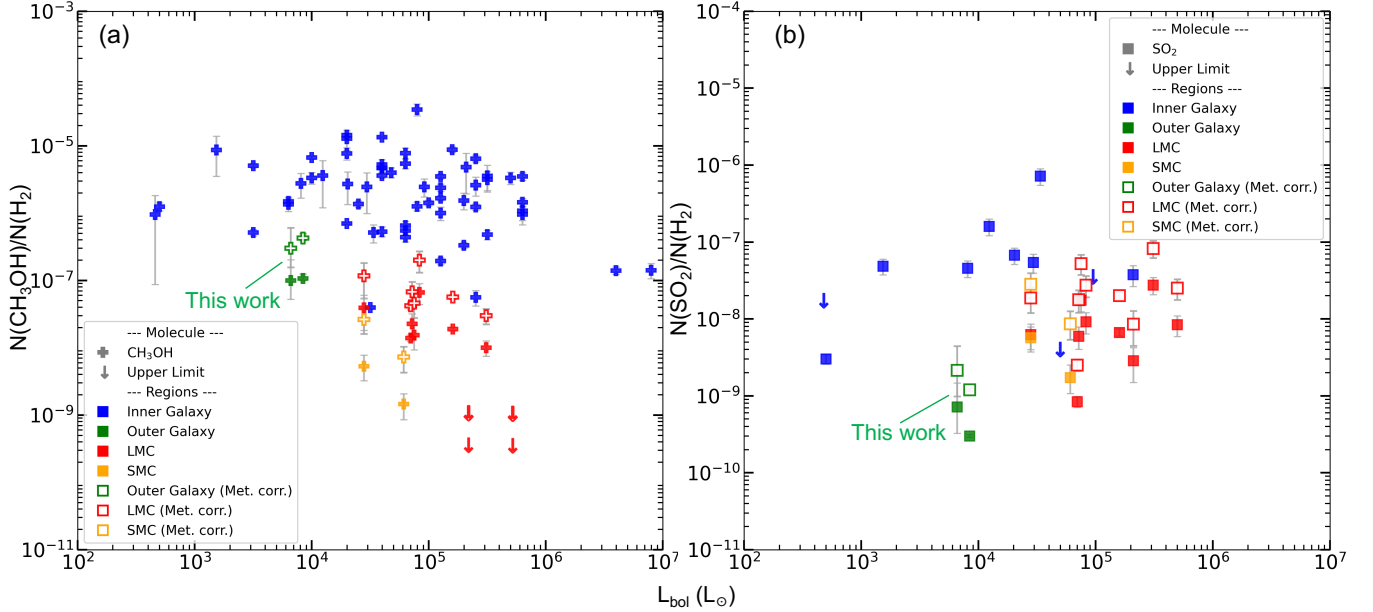


Figure 5. The $N(\text{CH}_3\text{OH})/N(\text{H}_2)$ (a) and $N(\text{SO}_2)/N(\text{H}_2)$ (b) ratios as a function of luminosities for the inner Galactic sources (blue; Fuente et al. 2014; Qin et al. 2022; van Gelder et al. 2022a; Santos et al. 2024; Chen et al. 2025; Li et al. 2025), the outer Galactic sources (green; Shimonishi et al. 2021), the LMC sources (red; Shimonishi et al. 2016, 2020, 2021, 2025; Sewilo et al. 2022; Hamedani Golshan et al. 2024; Broadmeadow et al. 2025), and the SMC sources (orange; Shimonishi et al. 2023). The open marks in white show the values corrected for metallicity for each low-metallicity source (e.g., multiplied by a factor of 3 for $Z = 1/3 Z_\odot$). The subscript arrows in each plot represent the upper limits.

(Shimonishi et al. 2020). On the other hand, the outer Galactic hot cores likely experienced environments similar to those of the inner Galactic sources during their initial ice-forming stages, allowing for the efficient formation of CH_3OH .

Figure 5(b) presents a comparison of the $N(\text{SO}_2)/N(\text{H}_2)$ ratios. This figure indicates that the $N(\text{SO}_2)/N(\text{H}_2)$ ratios of the inner Galactic sources are similar to the metallicity-corrected values of the Magellanic sources. In contrast, the median value for the outer Galactic sources is significantly lower than that of the inner Galactic sources by approximately a factor of 30. Although SO_2 is proposed as a reliable tracer for hot cores in the Magellanic Clouds (Shimonishi et al. 2020), a low SO_2 abundance in the outer Galactic hot core has been previously reported (Shimonishi et al. 2021). Such a low SO_2 abundance is also observed in this work, indicating that it might be a characteristic chemical property of hot cores in the outer Galaxy. SO_2 in hot cores is thought to form primarily through solid-phase reactions involving the oxidation of sulfur (S) by radicals (O or OH) or O_2 during the early stages of star formation (e.g., Santos et al. 2024). Although gas-phase production of SO_2 via the successive oxidation reaction of H_2S in warm gas also contributes to the observed column densities of SO_2 in hot cores (Charnley 1997; Nomura & Millar 2004), the SO_2 abundance in hot cores would strongly depend on the efficiency of these surface reactions. It is known that the cosmic ray intensity in the Galactic

anticenter region is lower than that in the inner Galaxy (Lipari & Vernetto 2025). Although the cosmic ray intensity in the outer Galaxy has not been directly constrained (as far as we know), it is expected to be lower than that in the inner Galaxy, considering their results and the lower star formation efficiency in the outer Galaxy. Since cosmic rays play a crucial role in generating radical species on dust grains via cosmic ray-induced UV photodissociation of water ice (e.g., Gaches & Viti 2025, and references therein), we speculate that the low SO_2 abundance in outer Galactic hot cores results from the insufficient production of oxidizing radicals (O and OH) in its weak cosmic ray environment.

This scenario contrasts with the situation in the Magellanic Clouds. In these regions, active star formation indicates a high cosmic ray intensity, which ensures an abundant supply of oxidizing radicals via the photodissociation of water ice, thereby enhancing SO_2 formation. Furthermore, unlike the precursor of CH_3OH (CO), the precursors of SO_2 (S and O) are thought to react within the water-rich ice matrix, which is thermally more stable than the CO-rich ice layer (Santos et al. 2024). This stability allows these precursors to reside on dust grains and undergo oxidation even under the warmer dust temperatures characteristic of the LMC, where CH_3OH formation is inhibited. Thus, while the CH_3OH abundance is critically sensitive to dust temperature during the initial ice-forming stages, the local cosmic ray intensity

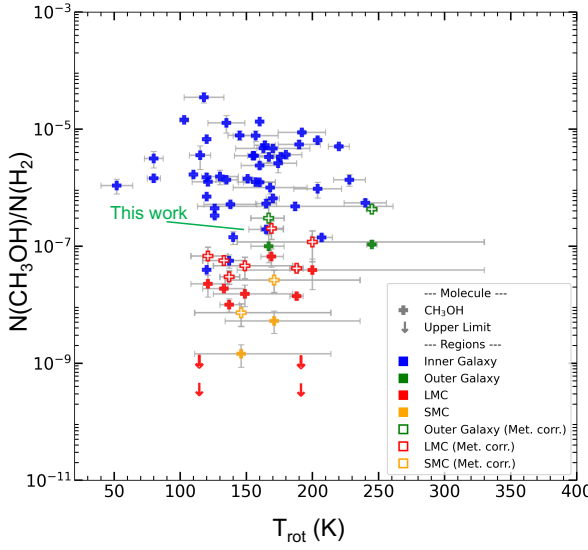


Figure 6. $N(\text{CH}_3\text{OH})/N(\text{H}_2)$ ratios as a function of rotational temperatures for the inner Galactic hot cores (blue; Fuente et al. 2014; Li et al. 2025; Chen et al. 2025), outer Galactic hot cores (green; Shimonishi et al. 2021), the LMC hot cores (red; Shimonishi et al. 2016, 2020, 2025; Broadmeadow et al. 2025), and SMC hot cores (orange; Shimonishi et al. 2023). The rotational temperatures are derived from the CH_3OH lines. For the inner Galactic sources whose rotational temperatures of CH_3OH did not be derived, rotational temperatures of the other COMs are used. For the LMC and SMC sources whose rotational temperatures of CH_3OH could not be derived, rotational temperatures of SO_2 are used. The open marks in white show the values corrected for metallicity for each low-metallicity hot core. The subscript arrows represent the upper limits.

likely plays a key role in determining the SO_2 abundance in hot cores.

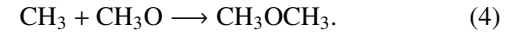
4.4. Molecular abundances: Focusing on COMs

Figure 7(a) and (b) show comparisons of the abundances of COMs (CH_3OCH_3 and $\text{C}_2\text{H}_5\text{OH}$) normalized by CH_3OH , and Panel (c) shows a comparison of the $N(\text{C}_2\text{H}_5\text{OH})/N(\text{CH}_3\text{OCH}_3)$ ratios among the hot cores in the inner Galaxy (blue), outer Galaxy (green), and LMC (red). D_{GC} of these inner Galactic sources ranges from ~ 0.2 to 8 kpc.

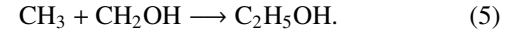
Panels (a) and (b) indicate that the $N(\text{CH}_3\text{OCH}_3)/N(\text{CH}_3\text{OH})$ and $N(\text{C}_2\text{H}_5\text{OH})/N(\text{CH}_3\text{OH})$ ratios of the inner Galactic and LMC sources are similar over a range of luminosities. For the outer Galactic sources, the $N(\text{CH}_3\text{OCH}_3)/N(\text{CH}_3\text{OH})$ ratios are somewhat lower compared to those of the inner Galactic sources ($\sim 1/9$ of the median of the inner Galactic ones), lying near the lower limit. The same applies to the $N(\text{C}_2\text{H}_5\text{OH})/N(\text{CH}_3\text{OH})$ ratio, as indicated by the other outer Galactic source (Shimonishi et al. 2021). Note that

$\text{C}_2\text{H}_5\text{OH}$ was not detected in this work, and only an upper limit was derived.

CH_3OCH_3 and $\text{C}_2\text{H}_5\text{OH}$ are widely believed to be daughter species of CH_3OH , and strong correlations between the column densities of these three species have been confirmed in recent observations of inner Galactic hot cores (Kou et al. 2025). Based on experimental studies, these molecules are primarily thought to form through the recombination of radicals, which are photodissociation products of CH_3OH (e.g., CH_2OH , CH_3O , and CH_3 ; Öberg et al. 2009; Bergantini et al. 2018). CH_3OCH_3 is formed by the recombination of CH_3 and CH_3O radicals (Bergantini et al. 2018):



$\text{C}_2\text{H}_5\text{OH}$ is formed by the recombination of CH_3 and CH_2OH radicals (Bergantini et al. 2018):

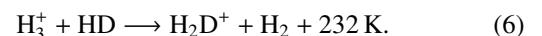


Considering these formation mechanisms, the lower abundances of these COMs in the outer Galactic sources are likely due to the lower cosmic ray intensity as discussed in Section 4.3, which suppresses the dissociation of CH_3OH into their precursor radicals.

On the other hand, the $N(\text{C}_2\text{H}_5\text{OH})/N(\text{CH}_3\text{OCH}_3)$ ratios shown in Panel (c) are similar among the sources in the inner Galaxy, outer Galaxy, and LMC. The values for the outer Galactic and LMC sources (0.38 and 0.77, respectively) are consistent with the median value of the inner Galactic sources (0.43) within a factor of 2. This remarkable similarity suggests a chemical link between these species, regardless of the differing interstellar environments. This implies that the formation mechanisms of these COMs in low-metallicity environments are similar to those in the inner Galactic regions, although their formation efficiencies would be somewhat affected by the local environmental conditions (e.g., cosmic ray intensity). To validate this hypothesis, it is crucial to increase the sample size of COM-rich hot cores in the outer Galaxy and the Magellanic Clouds to enable more robust statistical comparisons.

4.5. Deuterium fractionation

Deuterium chemistry serves as a crucial tool for deciphering the chemical and physical evolution of interstellar molecules (Caselli & Ceccarelli 2012; Ceccarelli et al. 2014). It is well established that deuterium fractionation occurs efficiently at low temperatures (e.g., Furuya et al. 2016). This efficiency arises from the exothermic nature of the key reaction driving deuterium fractionation (e.g., Watson 1974; Ceccarelli et al. 2014):



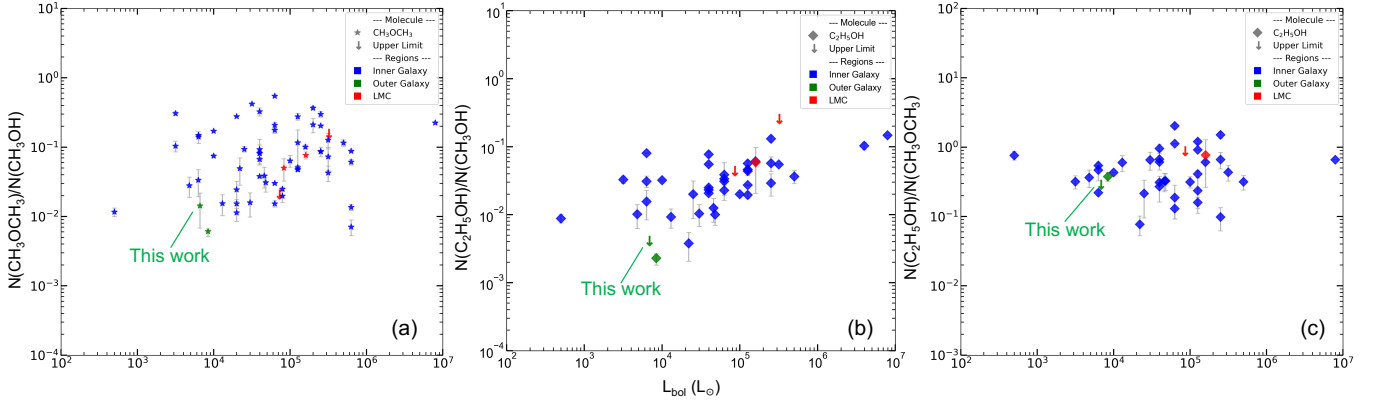


Figure 7. (a) $N(\text{CH}_3\text{OCH}_3)/N(\text{CH}_3\text{OH})$, (b) $N(\text{C}_2\text{H}_5\text{OH})/N(\text{CH}_3\text{OH})$, and (c) $N(\text{C}_2\text{H}_5\text{OH})/N(\text{CH}_3\text{OCH}_3)$ ratios as a function of luminosity. The symbols represent inner Galactic hot cores (blue; Fuente et al. 2014; Qin et al. 2022; Chen et al. 2023; Li et al. 2024, 2025; Kou et al. 2025), outer Galactic hot cores (green; Shimonishi et al. 2021), and LMC hot cores (red; Shimonishi et al. 2016, 2020; Broadmeadow et al. 2025). The subscript arrows in each plot represent the upper limits.

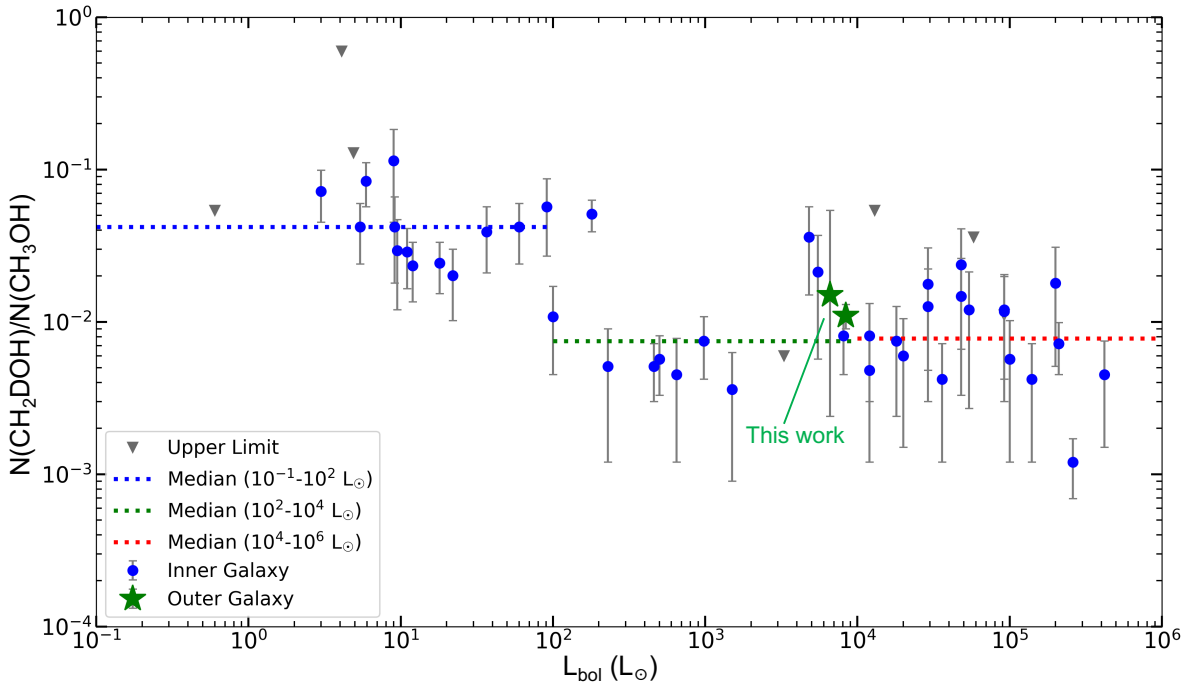


Figure 8. The $N(\text{CH}_2\text{DOH})/N(\text{CH}_3\text{OH})$ ratios as a function of luminosities for the inner Galactic sources (blue; Fuente et al. 2014; Belloche et al. 2016; Müller et al. 2016; Jørgensen et al. 2018; Taquet et al. 2019; Jacobsen et al. 2019; Martín-Doménech et al. 2019, 2021; Manigand et al. 2020; Yang et al. 2020; van Gelder et al. 2020, 2022a,b; Ligterink et al. 2021; Hsu et al. 2022; Drozdovskaya et al. 2022), and the outer Galactic sources (green; Shimonishi et al. 2021). We used the values of the inner Galactic $N(\text{CH}_2\text{DOH})/N(\text{CH}_3\text{OH})$ ratios summarized in van Gelder et al. (2022b). The dotted lines in different color show the median values of $N(\text{CH}_2\text{DOH})/N(\text{CH}_3\text{OH})$ ratio between each luminosity range (blue for 10^{-1} L_\odot - 10^2 L_\odot , green for 10^2 L_\odot - 10^4 L_\odot , and red for 10^4 L_\odot - 10^6 L_\odot). The subscript triangles represent the upper limits.

Since the backward reaction is significantly hindered below 20 K, H_2D^+ is enhanced in cold prestellar cores, leading to an increased atomic D/H ratio in the gas phase. Moreover, on dust surfaces, deuterium fractionation of CH_3OH and related species proceeds effectively under cold conditions via successive H-abstraction and D-substitution reactions (Hidaka et al. 2009; Riedel et al. 2023). These processes result in observed abundances of deuterated molecules (e.g., D_2CO and CH_2DOH) in star-forming regions that are orders of magnitude higher than the cosmic D/H ratio ($(1.52 \pm 0.08) \times 10^{-5}$; Linsky 2003).

The $N(\text{CH}_2\text{DOH})/N(\text{CH}_3\text{OH})$ ratio of Sh 2-283-1a SMM1 is $1.5^{+3.9}_{-1.2}\%$, which is comparable to that of the other outer Galactic hot core ($1.1 \pm 0.2\%$; Shimonishi et al. 2021). We also compare the $N(\text{CH}_2\text{DOH})/N(\text{CH}_3\text{OH})$ ratio with those of inner Galactic sources in Figure 8. In this figure, we plot the $N(\text{CH}_2\text{DOH})/N(\text{CH}_3\text{OH})$ ratios as a function of luminosity for each source. Blue symbols represent the values for inner Galactic sources, taken from van Gelder et al. (2022b). The plotted sources are limited to hot cores (or hot corinos) associated with warm gas ($\gtrsim 100$ K).

This figure indicates that the $N(\text{CH}_2\text{DOH})/N(\text{CH}_3\text{OH})$ ratios for low-mass sources are higher than those for intermediate- and high-mass sources, while the values for intermediate- and high-mass sources are similar to each other. The lower $N(\text{CH}_2\text{DOH})/N(\text{CH}_3\text{OH})$ ratios in high-mass sources are generally attributed to their higher temperatures during the prestellar phase and shorter prestellar timescales (van Gelder et al. 2022b; Sakai et al. 2025). For Sh 2-283-1a SMM1, the $N(\text{CH}_2\text{DOH})/N(\text{CH}_3\text{OH})$ ratio is comparable to those of intermediate- to high-mass inner Galactic sources. This result is consistent with its estimated luminosity ($\sim 6.7 \times 10^3 \text{ L}_\odot$). These results suggest that Sh 2-283-1a SMM1 experienced efficient deuterium fractionation during the formation of CH_3OH , which occurred under cold environmental conditions ($\lesssim 20$ K).

5. SUMMARY

We report the chemical analyses of the outer Galactic hot core, Sh 2-283-1a SMM1 ($D_{\text{GC}} = 15.7 \text{ kpc}$, $Z \sim 0.3 \text{ Z}_\odot$), based on ALMA observations. The main conclusions of this study are summarized below.

1. Toward Sh 2-283-1a SMM1, a variety of molecular species (carbon-, oxygen-, nitrogen-, sulfur-, and silicon-bearing species), including COMs, were detected at the emission peak of 0.87 mm continuum. The rotational diagram and continuum analyses revealed the presence of a warm ($T > 100$ K), dense ($n \sim 4 \times 10^6 \text{ cm}^{-3}$), and compact ($< 0.03 \text{ pc}$) region associated with the protostar ($\sim 6.7 \times 10^3 \text{ L}_\odot$).

2. A comparison of the molecular abundances relative to CH_3OH between the outer Galactic hot cores reveals a similarity, demonstrating that such chemically rich hot cores exist in different regions of the outer Galaxy.
3. A comparison of the $N(\text{CH}_3\text{OH})/N(\text{H}_2)$ ratios among the inner Galactic, outer Galactic, and Magellanic hot cores shows that the metallicity-corrected ratios of the outer Galactic hot cores resemble those of the inner Galactic hot cores. In contrast, the median value for the Magellanic hot cores is more than one order of magnitude lower than that of the inner Galactic hot cores. These results indicate that dust temperature during the initial ice-forming stages significantly affects the CH_3OH abundances in hot cores.
4. In contrast, the $N(\text{SO}_2)/N(\text{H}_2)$ ratio of the outer Galactic hot cores is significantly lower than that of the inner Galactic hot cores, whereas the values are comparable between the inner Galactic and Magellanic hot cores, indicating that cosmic ray intensity plays a key role in determining the formation efficiency of SO_2 .
5. The $N(\text{CH}_3\text{OCH}_3)/N(\text{CH}_3\text{OH})$ and $N(\text{C}_2\text{H}_5\text{OH})/N(\text{CH}_3\text{OH})$ ratios of the outer Galactic sources are moderately lower than those of the inner Galactic ones. This is likely due to the lower cosmic ray intensity in the outer Galaxy; these COMs are primarily thought to form via radical-radical reactions, and the precursor radicals are produced by the photodissociation of CH_3OH induced by cosmic rays. On the other hand, the $N(\text{C}_2\text{H}_5\text{OH})/N(\text{CH}_3\text{OCH}_3)$ ratios are similar among the inner Galactic, outer Galactic, and LMC sources, indicating the universality of the formation mechanisms of these molecules across the different environments.
6. The $N(\text{CH}_2\text{DOH})/N(\text{CH}_3\text{OH})$ ratio of Sh 2-283-1a SMM1 is $1.5^{+3.9}_{-1.2}\%$, which is comparable to that of another outer Galactic hot core and those of inner Galactic intermediate- to high-mass hot cores.

1 This paper makes use of the following ALMA data:
 2 ADS/JAO.ALMA#2022.1.01270.S. ALMA is a partnership
 3 of ESO (representing its member states), NSF (USA) and
 4 NINS (Japan), together with NRC (Canada), NSTC and
 5 ASIAA (Taiwan), and KASI (Republic of Korea), in coop-
 6 eration with the Republic of Chile. The Joint ALMA Ob-
 7 servatory is operated by ESO, AUI/NRAO and NAOJ. This
 8 work has made extensive use of the Cologne Database for
 9 Molecular Spectroscopy and the molecular database of the
 10 Jet Propulsion Laboratory. This work was supported by
 11 JSPS KAKENHI grant Nos. JP20H05845, JP21H00037, and
 12 JP21H01145. This work was supported by the Uchida En-
 13 ergy Science Promotion Foundation. T.I. was supported by
 14 the Niigata University Quantum Research Center (NU-Q).
 15 Finally, we would like to thank an anonymous referee for
 16 insightful comments, which substantially improved this pa-
 17 per.

REFERENCES

Arellano-Córdova, K. Z., Esteban, C., García-Rojas, J., & Méndez-Delgado, J. E. 2020a, MNRAS, 496, 1051, doi: [10.1093/mnras/staa1523](https://doi.org/10.1093/mnras/staa1523)
 —. 2020b, MNRAS, 496, 1051, doi: [10.1093/mnras/staa1523](https://doi.org/10.1093/mnras/staa1523)

Belloche, A., Müller, H. S. P., Garrod, R. T., & Menten, K. M. 2016, A&A, 587, A91, doi: [10.1051/0004-6361/201527268](https://doi.org/10.1051/0004-6361/201527268)

Bergantini, A., Góbi, S., Abplanalp, M. J., & Kaiser, R. I. 2018, ApJ, 852, 70, doi: [10.3847/1538-4357/aa9ce2](https://doi.org/10.3847/1538-4357/aa9ce2)

Bragança, G. A., Daflon, S., Lanz, T., et al. 2019, A&A, 625, A120, doi: [10.1051/0004-6361/201834554](https://doi.org/10.1051/0004-6361/201834554)

Broadmeadow, A., Sewiło, M., Mundy, L., et al. 2025, ApJ, 991, 59, doi: [10.3847/1538-4357/ade9ae](https://doi.org/10.3847/1538-4357/ade9ae)

CASA Team, Bean, B., Bhatnagar, S., et al. 2022, PASP, 134, 114501, doi: [10.1088/1538-3873/ac9642](https://doi.org/10.1088/1538-3873/ac9642)

Caselli, P., & Ceccarelli, C. 2012, A&A Rv, 20, 56, doi: [10.1007/s00159-012-0056-x](https://doi.org/10.1007/s00159-012-0056-x)

Ceccarelli, C., Caselli, P., Bockelée-Morvan, D., et al. 2014, in Protostars and Planets VI, ed. H. Beuther, R. S. Klessen, C. P. Dullemond, & T. Henning, 859, doi: [10.2458/azu_uapress_9780816531240-ch037](https://doi.org/10.2458/azu_uapress_9780816531240-ch037)

Charnley, S. B. 1997, ApJ, 481, 396

Chen, L., Qin, S.-L., Liu, T., et al. 2025, A&A, 694, A166, doi: [10.1051/0004-6361/202452598](https://doi.org/10.1051/0004-6361/202452598)

Chen, Y., van Gelder, M. L., Nazari, P., et al. 2023, A&A, 678, A137, doi: [10.1051/0004-6361/202346491](https://doi.org/10.1051/0004-6361/202346491)

Cox, A. N. 2000, Allen's astrophysical quantities (Springer)

Drozdovskaya, M. N., Coudert, L. H., Margulès, L., et al. 2022, A&A, 659, A69, doi: [10.1051/0004-6361/202142863](https://doi.org/10.1051/0004-6361/202142863)

Elia, D., Molinari, S., Schisano, E., et al. 2022, ApJ, 941, 162, doi: [10.3847/1538-4357/aca27d](https://doi.org/10.3847/1538-4357/aca27d)

Fernández-Martín, A., Pérez-Montero, E., Vílchez, J. M., & Mampaso, A. 2017, A&A, 597, A84, doi: [10.1051/0004-6361/201628423](https://doi.org/10.1051/0004-6361/201628423)

Fich, M., & Silkey, M. 1991, ApJ, 366, 107, doi: [10.1086/169544](https://doi.org/10.1086/169544)

Fuente, A., Cernicharo, J., Caselli, P., et al. 2014, A&A, 568, A65, doi: [10.1051/0004-6361/201323074](https://doi.org/10.1051/0004-6361/201323074)

Furuya, K., van Dishoeck, E. F., & Aikawa, Y. 2016, A&A, 586, A127, doi: [10.1051/0004-6361/201527579](https://doi.org/10.1051/0004-6361/201527579)

Gaches, B. A. L., & Viti, S. 2025, arXiv e-prints, arXiv:2512.10060, doi: [10.48550/arXiv.2512.10060](https://doi.org/10.48550/arXiv.2512.10060)

Gaia Collaboration, Brown, A. G. A., Vallenari, A., et al. 2021, A&A, 649, A1, doi: [10.1051/0004-6361/202039657](https://doi.org/10.1051/0004-6361/202039657)

Garrod, R. T., & Herbst, E. 2006, A&A, 457, 927, doi: [10.1051/0004-6361:20065560](https://doi.org/10.1051/0004-6361:20065560)

Goldsmith, P. F., & Langer, W. D. 1999, ApJ, 517, 209, doi: [10.1086/307195](https://doi.org/10.1086/307195)

Graczyk, D., Pietrzyński, G., Thompson, I. B., et al. 2020, ApJ, 904, 13, doi: [10.3847/1538-4357/abb2b](https://doi.org/10.3847/1538-4357/abb2b)

Hamedani Golshan, R., Sánchez-Monge, Á., Schilke, P., et al. 2024, A&A, 688, A3, doi: [10.1051/0004-6361/202349077](https://doi.org/10.1051/0004-6361/202349077)

Herbst, E., & van Dishoeck, E. F. 2009, ARA&A, 47, 427, doi: [10.1146/annurev-astro-082708-101654](https://doi.org/10.1146/annurev-astro-082708-101654)

Hidaka, H., Watanabe, M., Kouchi, A., & Watanabe, N. 2009, ApJ, 702, 291, doi: [10.1088/0004-637X/702/1/291](https://doi.org/10.1088/0004-637X/702/1/291)

Hsu, S.-Y., Liu, S.-Y., Liu, T., et al. 2022, ApJ, 927, 218, doi: [10.3847/1538-4357/ac49e0](https://doi.org/10.3847/1538-4357/ac49e0)

Ikeda, T., Shimonishi, T., Izumi, N., et al. 2025, *ApJ*, 988, 111, doi: [10.3847/1538-4357/ade235](https://doi.org/10.3847/1538-4357/ade235)

Jacobsen, S. K., Jørgensen, J. K., Di Francesco, J., et al. 2019, *A&A*, 629, A29, doi: [10.1051/0004-6361/201833214](https://doi.org/10.1051/0004-6361/201833214)

Jørgensen, J. K., Müller, H. S. P., Calcutt, H., et al. 2018, *A&A*, 620, A170, doi: [10.1051/0004-6361/201731667](https://doi.org/10.1051/0004-6361/201731667)

Kou, Z., Li, X., Qin, S.-L., et al. 2025, *MNRAS*, 538, 2579, doi: [10.1093/mnras/staf408](https://doi.org/10.1093/mnras/staf408)

Kurtz, S., Cesaroni, R., Churchwell, E., Hofner, P., & Walmsley, C. M. 2000, in *Protostars and Planets IV*, ed. V. Mannings, A. P. Boss, & S. S. Russell, 299–326

Li, C., Qin, S.-L., Liu, T., et al. 2024, *MNRAS*, 533, 1583, doi: [10.1093/mnras/stae1934](https://doi.org/10.1093/mnras/stae1934)

Li, Z.-Y., Liu, X., Liu, T., et al. 2025, *A&A*, 697, A190, doi: [10.1051/0004-6361/202452762](https://doi.org/10.1051/0004-6361/202452762)

Ligterink, N. F. W., Ahmadi, A., Coutens, A., et al. 2021, *A&A*, 647, A87, doi: [10.1051/0004-6361/202039619](https://doi.org/10.1051/0004-6361/202039619)

Linsky, J. L. 2003, *SSRv*, 106, 49, doi: [10.1023/A:1024673217736](https://doi.org/10.1023/A:1024673217736)

Lipari, P., & Vernetto, S. 2025, arXiv e-prints, arXiv:2509.09028, doi: [10.48550/arXiv.2509.09028](https://doi.org/10.48550/arXiv.2509.09028)

Manigand, S., Jørgensen, J. K., Calcutt, H., et al. 2020, *A&A*, 635, A48, doi: [10.1051/0004-6361/201936299](https://doi.org/10.1051/0004-6361/201936299)

Martín-Doménech, R., Bergner, J. B., Öberg, K. I., & Jørgensen, J. K. 2019, *ApJ*, 880, 130, doi: [10.3847/1538-4357/ab2a08](https://doi.org/10.3847/1538-4357/ab2a08)

Martín-Doménech, R., Bergner, J. B., Öberg, K. I., et al. 2021, *ApJ*, 923, 155, doi: [10.3847/1538-4357/ac26b9](https://doi.org/10.3847/1538-4357/ac26b9)

Milam, S. N., Savage, C., Brewster, M. A., Ziurys, L. M., & Wyckoff, S. 2005, *ApJ*, 634, 1126, doi: [10.1086/497123](https://doi.org/10.1086/497123)

Müller, H. S. P., Schröder, F., Stutzki, J., et al. 2005, in *Astrochemistry: Recent Successes and Current Challenges*, ed. D. C. Lis, G. A. Blake, & E. Herbst, Vol. 231, 62

Müller, H. S. P., Thorwirth, S., Roth, D. A., & Winnewisser, G. 2001, *A&A*, 370, L49, doi: [10.1051/0004-6361:20010367](https://doi.org/10.1051/0004-6361:20010367)

Müller, H. S. P., Belloche, A., Xu, L.-H., et al. 2016, *A&A*, 587, A92, doi: [10.1051/0004-6361/201527470](https://doi.org/10.1051/0004-6361/201527470)

Nakanishi, H., & Sofue, Y. 2016, *PASJ*, 68, 5, doi: [10.1093/pasj/psv108](https://doi.org/10.1093/pasj/psv108)

Nomura, H., & Millar, T. J. 2004, *A&A*, 414, 409, doi: [10.1051/0004-6361:20031646](https://doi.org/10.1051/0004-6361:20031646)

Öberg, K. I., Garrod, R. T., van Dishoeck, E. F., & Linnartz, H. 2009, *A&A*, 504, 891, doi: [10.1051/0004-6361/200912559](https://doi.org/10.1051/0004-6361/200912559)

Ossenkopf, V., & Henning, T. 1994, *A&A*, 291, 943

Pickett, H. M., Poynter, R. L., Cohen, E. A., et al. 1998, *JQSRT*, 60, 883, doi: [10.1016/S0022-4073\(98\)00091-0](https://doi.org/10.1016/S0022-4073(98)00091-0)

Pietrzyński, G., Graczyk, D., Gieren, W., et al. 2013, *Nature*, 495, 76, doi: [10.1038/nature11878](https://doi.org/10.1038/nature11878)

Qin, S.-L., Liu, T., Liu, X., et al. 2022, *MNRAS*, 511, 3463, doi: [10.1093/mnras/stac219](https://doi.org/10.1093/mnras/stac219)

Reid, M. J., Menten, K. M., Brunthaler, A., et al. 2019, *ApJ*, 885, 131, doi: [10.3847/1538-4357/ab4a11](https://doi.org/10.3847/1538-4357/ab4a11)

Riedel, W., Sipilä, O., Redaelli, E., et al. 2023, *A&A*, 680, A87, doi: [10.1051/0004-6361/202245367](https://doi.org/10.1051/0004-6361/202245367)

Sakai, T., Shiomura, N., Sanhueza, P., et al. 2025, *ApJ*, 983, 37, doi: [10.3847/1538-4357/adbaf5a](https://doi.org/10.3847/1538-4357/adbaf5a)

Santos, J. C., van Gelder, M. L., Nazari, P., Ahmadi, A., & van Dishoeck, E. F. 2024, *A&A*, 689, A248, doi: [10.1051/0004-6361/202450736](https://doi.org/10.1051/0004-6361/202450736)

Sewiło, M., Indebetouw, R., Charnley, S. B., et al. 2018, *ApJL*, 853, L19, doi: [10.3847/2041-8213/aaa079](https://doi.org/10.3847/2041-8213/aaa079)

Sewiło, M., Cordiner, M., Charnley, S. B., et al. 2022, *ApJ*, 931, 102, doi: [10.3847/1538-4357/ac4e8f](https://doi.org/10.3847/1538-4357/ac4e8f)

Shimonishi, T. 2024, arXiv e-prints, arXiv:2411.04451, doi: [10.48550/arXiv.2411.04451](https://doi.org/10.48550/arXiv.2411.04451)

Shimonishi, T., Das, A., Sakai, N., et al. 2020, *ApJ*, 891, 164, doi: [10.3847/1538-4357/ab6e6b](https://doi.org/10.3847/1538-4357/ab6e6b)

Shimonishi, T., Izumi, N., Furuya, K., & Yasui, C. 2021, *ApJ*, 922, 206, doi: [10.3847/1538-4357/ac289b](https://doi.org/10.3847/1538-4357/ac289b)

Shimonishi, T., Onaka, T., Kawamura, A., & Aikawa, Y. 2016, *ApJ*, 827, 72, doi: [10.3847/0004-637X/827/1/72](https://doi.org/10.3847/0004-637X/827/1/72)

Shimonishi, T., Tanaka, K. E. I., Zhang, Y., & Furuya, K. 2023, *ApJL*, 946, L41, doi: [10.3847/2041-8213/acc031](https://doi.org/10.3847/2041-8213/acc031)

Shimonishi, T., Tanaka, K. E. I., Zhang, Y., et al. 2025, arXiv e-prints, arXiv:2512.15983. <https://arxiv.org/abs/2512.15983>

Sun, Y., Yang, J., Zhang, S., et al. 2024, *ApJL*, 977, L35, doi: [10.3847/2041-8213/ad9605](https://doi.org/10.3847/2041-8213/ad9605)

Sutton, E. C., Peng, R., Danchi, W. C., et al. 1995, *ApJS*, 97, 455, doi: [10.1086/192147](https://doi.org/10.1086/192147)

Taquet, V., Bianchi, E., Codella, C., et al. 2019, *A&A*, 632, A19, doi: [10.1051/0004-6361/201936044](https://doi.org/10.1051/0004-6361/201936044)

van Dishoeck, E. F., & Blake, G. A. 1998, *ARA&A*, 36, 317, doi: [10.1146/annurev.astro.36.1.317](https://doi.org/10.1146/annurev.astro.36.1.317)

van Gelder, M. L., Tabone, B., Tychoniec, Ł., et al. 2020, *A&A*, 639, A87, doi: [10.1051/0004-6361/202037758](https://doi.org/10.1051/0004-6361/202037758)

van Gelder, M. L., Nazari, P., Tabone, B., et al. 2022a, *A&A*, 662, A67, doi: [10.1051/0004-6361/202142769](https://doi.org/10.1051/0004-6361/202142769)

van Gelder, M. L., Jaspers, J., Nazari, P., et al. 2022b, *A&A*, 667, A136, doi: [10.1051/0004-6361/202244471](https://doi.org/10.1051/0004-6361/202244471)

Watanabe, N., & Kouchi, A. 2002, *ApJL*, 571, L173, doi: [10.1086/341412](https://doi.org/10.1086/341412)

Watson, W. D. 1974, *ApJ*, 188, 35, doi: [10.1086/152681](https://doi.org/10.1086/152681)

Wenger, T. V., Balser, D. S., Anderson, L. D., & Bania, T. M. 2019, *ApJ*, 887, 114, doi: [10.3847/1538-4357/ab53d3](https://doi.org/10.3847/1538-4357/ab53d3)

Wolfire, M. G., McKee, C. F., Hollenbach, D., & Tielens, A. G. M. 2003, *The Astrophysical Journal*, 587, 278, doi: [10.1086/368016](https://doi.org/10.1086/368016)

Yan, Y. T., Henkel, C., Kobayashi, C., et al. 2023, *A&A*, 670, A98, doi: [10.1051/0004-6361/202244584](https://doi.org/10.1051/0004-6361/202244584)

Yang, Y.-L., Evans, II, N. J., Smith, A., et al. 2020, *ApJ*, 891, 61, doi: [10.3847/1538-4357/ab7201](https://doi.org/10.3847/1538-4357/ab7201)

APPENDIX

A. THE ALMA SPECTRA OF THE DETECTED MOLECULAR EMISSION LINES

Figure A1 shows the ALMA spectra of the detected molecular lines. The blue solid lines in each spectrum represent the results of the Gaussian fitting.

B. THE MOLECULAR ABUNDANCES OF HOT CORES ACROSS THE GALAXY

Figure B2 plots the molecular abundances (CH_3OH and SO_2) as a function of D_{GC} . The dotted lines in each panel denote the Galactic gradient of the elemental abundances of C and S measured in H_{II} regions (Fernández-Martín et al. 2017; Arellano-Córdova et al. 2020a). The intercepts of these gradients are divided by 250 and 1000 for C and S, respectively. The plotted Galactic sources are the same as in Figure 5.

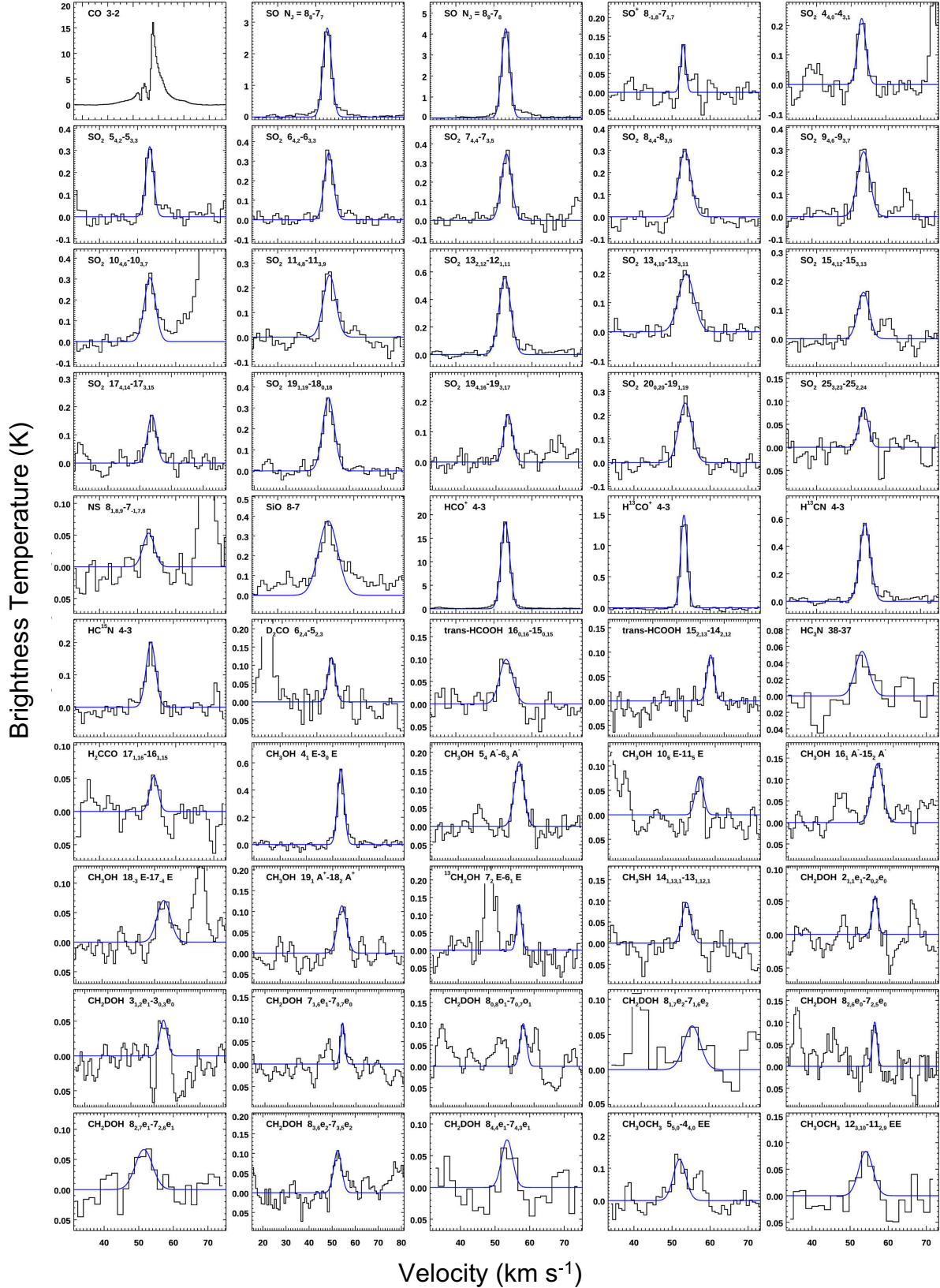


Figure A1. ALMA spectra of the detected molecular lines. The blue lines represent the result of fitting with Gaussian profiles. For the molecular species which multiple lines are detected, we sort them with the order of the upper state energy. For the CO($J = 3-2$) line, the integrated intensity is derived by directly integrating the spectra.

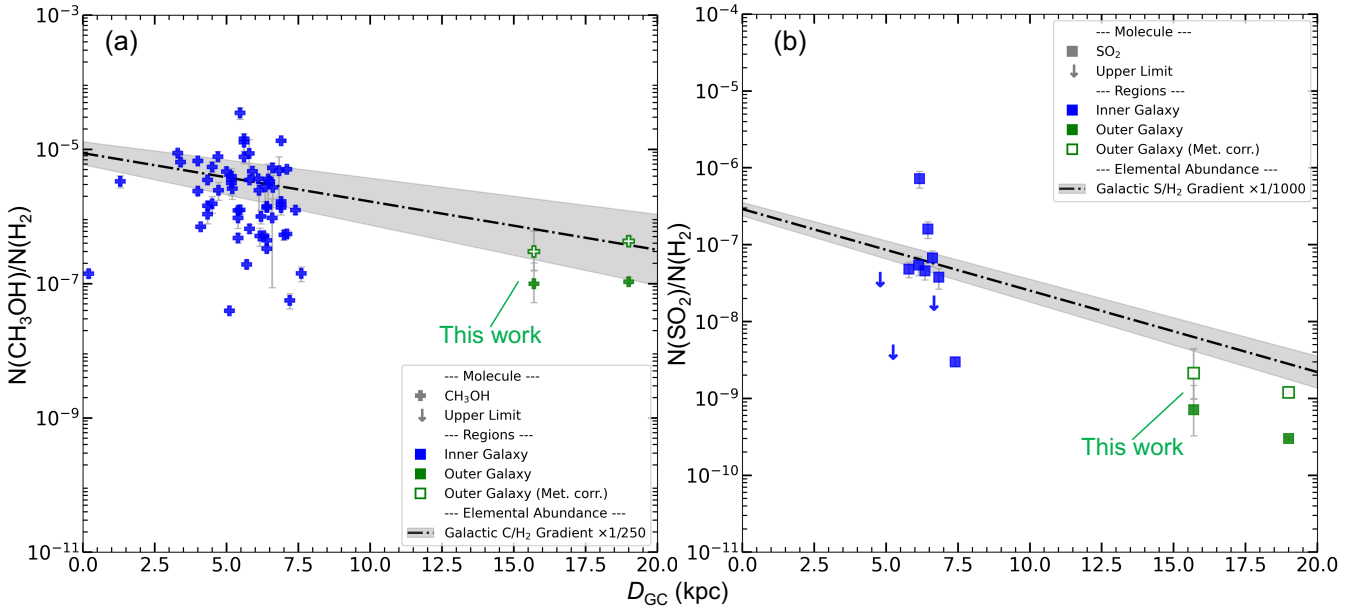


Figure B2. The $N(CH_3OH)/N(H_2)$ (a) and $N(SO_2)/N(H_2)$ (b) ratios as a function of D_{GC} for the inner Galaxy sources (blue; Fuente et al. 2014; van Gelder et al. 2022a; Santos et al. 2024; Chen et al. 2025; Li et al. 2025) and the outer Galactic sources (green; Shimonishi et al. 2021). The open white marks show the metallicity-corrected values for the low-metallicity sources. The dotted lines in each panel show the Galactic gradients of the elemental abundances of C (Arellano-Córdova et al. 2020b) and S (Fernández-Martín et al. 2017) relative to H₂. The intercepts of these gradients are divided by 250 and 1000 for C and S, respectively. The gray shaded regions in each panel show the error range of the gradients.